The Journal of Chemical Physics ARTICLE scitation.org/journal/jcp

Excited-state electronic structure of molecules using many-body Green's functions: Quasiparticles and electron–hole excitations with VOTCA-XTP

Cite as: J. Chem. Phys. 152, 114103 (2020); doi: 10.1063/1.5144277
Submitted: 30 December 2019 • Accepted: 24 February 2020 •
Published Online: 16 March 2020

G. Tirimbò,[1,2] V. Sundaram,[1,2] O. Çaylak,[1,2,3] W. Scharpach,[1,2] J. Sijen,[1,2] C. Junghans,[4] J. Brown,[4,5,6,7] F. Zapata Ruiz,[8] N. Renaud,[8] J. Wehner,[1,2] and B. Baumeier[1,2,a)]

AFFILIATIONS

[1] Department of Mathematics and Computer Science, Eindhoven University of Technology, P.O. Box 513, 5600 MB Eindhoven, The Netherlands
[2] Institute for Complex Molecular Systems, Eindhoven University of Technology, P.O. Box 513, 5600 MB Eindhoven, The Netherlands
[3] Institute for Pure and Applied Mathematics, University of California Los Angeles, 460 Portola Plaza, Los Angeles, California 90095, USA
[4] Computer, Computational, and Statistical Sciences Division, Los Alamos National Laboratory, Los Alamos, New Mexico 87545, USA
[5] Deptartment of Electrical Computer and Energy Engineering, University of Colorado Boulder, 425 UCB, Boulder, Colorado 80309, USA
[6] Renewable and Sustainable Energy Institute, University of Colorado Boulder, 4001 Discovery Dr., Boulder, Colorado 80303, USA
[7] Physics and Chemistry of Materials Group, Los Alamos National Laboratory, Los Alamos, New Mexico 87545, USA
[8] Netherlands eScience Center, Science Park 140, 1098 XG Amsterdam, The Netherlands

Note: This article is part of the JCP Special Topic on Electronic Structure Software.
[a)] **Author to whom correspondence should be addressed:** B.Baumeier@tue.nl. **URL:** https://www.baumeiergroup.com

ABSTRACT

We present the open-source VOTCA-XTP software for the calculation of the excited-state electronic structure of molecules using many-body Green's function theory in the *GW* approximation with the Bethe–Salpeter equation (BSE). This work provides a summary of the underlying theory and discusses the details of its implementation based on Gaussian orbitals, including resolution-of-identity techniques and different approaches to the frequency integration of the self-energy or acceleration by offloading compute-intensive matrix operations using graphics processing units in a hybrid OpenMP/Cuda scheme. A distinctive feature of VOTCA–XTP is the capability to couple the calculation of electronic excitations to a classical polarizable environment on an atomistic level in a coupled quantum- and molecular-mechanics (QM/MM) scheme, where a complex morphology can be imported from Molecular Dynamics simulations. The capabilities and limitations of the *GW*–BSE implementation are illustrated with two examples. First, we study the dependence of optically active electron–hole excitations in a series of diketopyrrolopyrrole-based oligomers on molecular-architecture modifications and the number of repeat units. Second, we use the *GW*–BSE/MM setup to investigate the effect of polarization on localized and intermolecular charge-transfer excited states in morphologies of low-donor content rubrene–fullerene mixtures. These showcases demonstrate that our implementation currently allows us to treat systems with up to 2500 basis functions on regular shared-memory workstations, providing accurate descriptions of quasiparticle and coupled electron–hole excited states of various characters on an equal footing.

I. INTRODUCTION

The functional role of molecules in either fabricated devices, such as organic light-emitting diodes,[1,2] photovoltaic cells,[3,4] and photodetectors,[5] or in naturally occurring mechanisms[6,7] is determined by characteristics of their electronically excited states. In many cases, the focus lies on dynamical processes, such as the diffusion of a photoexcited state, its conversion into free charges (or vice versa), or drift-diffusion of carriers. While an adequate description of such dynamics depends on the specifics of material composition and/or operating conditions in a device, basic understanding and control of the processes are often sought via analysis of the excited-state electronic structure in terms of energy levels or state diagrams.[8] In this context, gaining insight into first-principles calculations requires methods that reliably predict properties for a variety of excited states, ranging from single-particle, ionizing excitations to coupled electron–hole pairs on one or more molecules. Methods also need to be practical, in the sense that they can be applied to molecular complexes of the size relevant for the aforementioned applications at a manageable computational cost. Finding the appropriate balance between computational cost and accuracy plays a crucial role in analyzing large complex systems.

Post-Hartree–Fock wave function-based approaches, such as coupled cluster or configuration interaction, can generally be used to determine excited-state properties with good accuracy.[9–12] However, their large baseline computational cost and rapid scaling with the system size make the study of large molecular systems practically impossible in many situations. In contrast, density functional theory[13] (DFT) is commonly used to calculate ground-state properties, while the properties of non-ionizing excitations are formally accessible by its time-dependent (TD-DFT) extension.[14,15] While the computational effort of both techniques is moderate compared to the wave-function approaches, they rely on the choice of an approximate exchange-correlation functional. Separate calculations are necessary to determine reliable ionization energies, and the quality of predictions of different excited states, in particular, of charge-transfer (CT) character, is sensitive to the functional choice.[16–18]

Recently, the use of many-body Green's function theory,[15,19–21] typically more rooted in the solid-state community, has received increasing attention in quantum-chemical applications.[22–34] It consists of a two-step procedure in which, at first, the addition and removal of an electron are calculated within the *GW* approximation as quasiparticle (QP) excitations to an *N*-electron (DFT) ground state. In the second step, neutral excitations are constructed in the same framework as coupled electron–hole pairs by solving the so-called Bethe–Salpeter Equation (BSE).[15,35] Many-body effects, or electron correlation, are taken into account via a non-local, energy-dependent electron self-energy operator.[36] This *GW*–BSE method has been shown to yield excitation energies with good accuracy for different types of excitations, e.g., localized (Frenkel) and bimolecular CT excitons,[25,26] on an equal footing. The computational cost of *GW*–BSE is comparable to linear-response TD-DFT in the Casida formulation,[37] which makes it an attractive technique for the calculation of the excited-state electronic structure of complex molecular materials—provided that adequate software tools are available. Most common implementations stem from the solid-state community and use a plane-wave basis with periodic boundary conditions. While it is possible to study molecules by choosing a large unit cell in such calculations, this is computationally inefficient.

In this paper, we present an open-source implementation of *GW*–BSE in the VOTCA–XTP package[38] that expresses the electronic states using atom-centered Gaussian-type orbitals (GTOs). VOTCA–XTP is part of the VOTCA software suite,[39–41] written in C++, and freely available on GitHub. It contains an internal module for calculating the DFT ground state mostly for developmental purposes and additionally provides extensible interfaces to standard packages (Gaussian,[42] NWChem,[43] and ORCA[44]). One distinct feature of the *GW*–BSE implementation in VOTCA–XTP is that it comes in two modes. The standalone mode operates like any common quantum-chemistry software and requires only the atom coordinates of the molecule and calculation parameters as input. In the second mode, a complex molecular morphology of a solute–solvent mixture or a donor–acceptor blend is first simulated by Molecular Dynamics (MD) or similar techniques and then translated as a whole into an internal data structure. This morphology mode facilitates the evaluation of the excited-state electronic structure in a complex environment[41,45–48] in a hybrid quantum- and molecular-mechanics (QM/MM) *GW*–BSE/MM scheme[41] and is linked to a multiscale framework for the determination of dynamical electronic properties. Additional features of this framework include the calculation of electronic[49] and excitonic[50] intermolecular coupling elements (transfer integrals), the prediction of ultraviolet photoelectron spectra including carrier-vibration coupling,[48] the simulation of optical absorption and emission spectra from coupled solute–solvent relaxation,[51] and the determination of charge-carrier mobilities[40] and exciton diffusion lengths[52] via kinetic Monte Carlo.

Here, we give a concise overview of the underlying theory and details of the implementation, including the use of resolution-of-identity (RI) techniques, different approaches to the frequency integration of the self-energy, or acceleration by offloading compute-intensive matrix operations using graphics processing units (GPUs) in a hybrid OpenMP/Cuda scheme. We highlight VOTCA–XTP's capabilities using two showcase applications related to organic photovoltaics. The first one uses the standalone mode and comprises a study of the lowest optically active excitations in a series of diketopyrrolopyrrole-derived (DPP) oligomers depending on molecular-architecture modifications and the number of repeat units. DPP polymers are used as donor materials in bulk heterojunctions with a fullerene acceptor.[53–55] The polymeric nature of the material allows a systematic demonstration of the accessible system sizes and the computational cost involved. At the same time, this study yields insight into the effects of different approximations on the excitation energies and the localization behavior of the photoexcited electron–hole pair. The second case study uses the morphology mode to illustrate the importance of accounting for environment effects on excited states.[26] We consider a low-donor content amorphous mixture of rubrene and C_{60} as a realistic model system for a small-molecule donor–acceptor blend.[56] Particular focus lies here on evaluating the effects of atomistic polarization on single-molecule localized Frenkel and bimolecular CT excitons in different variants of the *GW*–BSE/MM setup.

This paper is organized as follows: In Sec. II, we briefly summarize the essential theoretical aspects underlying *GW*–BSE, while technical details of the implementation as well as software development strategies are discussed in Sec. III. In Sec. IV, we demonstrate

the capabilities of VOTCA–XTP in two examples: the size dependence of electronic excitations in the DPP family of polymers and the stabilization of CT excitations in rubrene–C_{60} mixtures due to environment polarization. Finally, we outline current limitations and future development directions in Sec. V.

II. THEORY

For the sake of compactness, we restrict the following discussion of the main concepts underlying *GW*–BSE to a spin-singlet, closed-shell system of N electrons. Using DFT, the ground state $|N, 0\rangle$ is determined from the solutions of the Kohn–Sham (KS) equations,[57]

$$\widehat{H}^{\mathrm{KS}}\left|\phi_i^{\mathrm{KS}}\right\rangle = [\widehat{H}_0 + \widehat{V}_{\mathrm{xc}}]\left|\phi_i^{\mathrm{KS}}\right\rangle = \varepsilon_i^{\mathrm{KS}}\left|\phi_i^{\mathrm{KS}}\right\rangle. \tag{1}$$

Here, $\widehat{H}_0 = \widehat{T}_0 + \widehat{V}_{\mathrm{ext}} + \widehat{V}_{\mathrm{H}}$, with $\widehat{T}_0$ being the kinetic energy, $\widehat{V}_{\mathrm{ext}}$ being an external potential, $\widehat{V}_{\mathrm{H}}$ being the Hartree potential, and $\widehat{V}_{\mathrm{xc}}$ being the exchange-correlation potential.

Excitations that add ($N \to N + 1$) or remove ($N \to N - 1$) an electron from the system, referred to as quasiparticles (QPs), are determined by using the one-particle Green's function,[19,58]

$$G_1(\boldsymbol{r}_1, t_1, \boldsymbol{r}_2, t_2) = -\mathrm{i}\langle N, 0|\widehat{\mathcal{T}}(\widehat{\psi}(\boldsymbol{r}_1, t_1)\widehat{\psi}^{\dagger}(\boldsymbol{r}_2, t_2))|N, 0\rangle, \tag{2}$$

where $\widehat{\mathcal{T}}$ is the time-ordering operator, and $\widehat{\psi}$ and $\widehat{\psi}^{\dagger}$ are the annihilation and the creation electron field operators, respectively. This Green's function obeys a Dyson-type equation of motion, which reads in spectral representation as

$$[\widehat{H}_0 + \widehat{\Sigma}(E)]G_1(E) = E\,G_1(E), \tag{3}$$

where the electron self-energy operator $\widehat{\Sigma}(E)$ contains the exchange-correlation effects. This equation is part of a closed set of coupled equations known as Hedin's equations.[35,59] An approximate solution to this system is provided by the *GW* approximation, in which the self-energy takes the form

$$\Sigma(\boldsymbol{r}, \boldsymbol{r}', \omega) = \frac{\mathrm{i}}{2\pi}\int \mathrm{d}\omega'\, G_1\left(\boldsymbol{r}, \boldsymbol{r}', \omega + \omega'\right)W\left(\boldsymbol{r}, \boldsymbol{r}', \omega\right), \tag{4}$$

i.e., it is a convolution of G_1 with the screened Coulomb interaction $W = \epsilon^{-1}v_{\mathrm{c}}$, where $v_{\mathrm{c}}(\boldsymbol{r}, \boldsymbol{r}') = |\boldsymbol{r} - \boldsymbol{r}'|^{-1}$ is the bare Coulomb interaction and $\epsilon^{-1}(\boldsymbol{r}, \boldsymbol{r}', \omega)$ is the inverse dielectric function calculated in the Random-Phase Approximation (RPA).[20]

Using this approximation, Eq. (3) is converted into a Dyson-type equation of motion for the quasiparticles (i.e., the QP electron and hole states),[23,60]

$$\left[\widehat{H}_0 + \widehat{\Sigma}(\varepsilon_i^{\mathrm{QP}})\right]\left|\phi_i^{\mathrm{QP}}\right\rangle = \varepsilon_i^{\mathrm{QP}}\left|\phi_i^{\mathrm{QP}}\right\rangle, \tag{5}$$

where $\varepsilon_i^{\mathrm{QP}}$ are the one-particle excitation energies of the system and $\left|\phi_i^{\mathrm{QP}}\right\rangle$ are the QP wave functions.

In practice, the QP wave functions are expressed in a basis of KS states, i.e., $\left|\phi_i^{\mathrm{QP}}\right\rangle = \sum_j a_j^i\left|\phi_j^{\mathrm{KS}}\right\rangle$. With $\widehat{H}_0 = \widehat{H}^{\mathrm{KS}} - \widehat{V}_{\mathrm{xc}}$, diagonalizing the energy-dependent QP Hamiltonian in this basis as

$$H_{ij}^{\mathrm{QP}}(E) = \varepsilon_i^{\mathrm{KS}}\delta_{ij} + \left\langle\phi_i^{\mathrm{KS}}\middle|\widehat{\Sigma}(E) - \widehat{V}_{\mathrm{xc}}\middle|\phi_j^{\mathrm{KS}}\right\rangle \tag{6}$$

yields the QP states and energies.

If the off-diagonal elements of Eq. (6) are small, i.e., $\left|\phi_i^{\mathrm{QP}}\right\rangle \approx \left|\phi_i^{\mathrm{KS}}\right\rangle$, the quasiparticle energies can be evaluated perturbatively according to

$$\varepsilon_i^{\mathrm{QP}} = \varepsilon_i^{\mathrm{KS}} + \Delta\varepsilon_i^{GW} = \varepsilon_i^{\mathrm{KS}} + \left\langle\phi_i^{\mathrm{KS}}\middle|\widehat{\Sigma}(\varepsilon_i^{\mathrm{QP}}) - \widehat{V}_{\mathrm{xc}}\middle|\phi_i^{\mathrm{KS}}\right\rangle. \tag{7}$$

Computing $\varepsilon_i^{\mathrm{QP}}$ requires the determination of $\Delta\varepsilon_i^{GW}$, which consequently leads to self-consistently solving Eq. (7). This can be achieved by first identifying an interval containing a solution on a grid and then refining this using a bisection (graphical solution). As an alternative, Newton fixed-point iterations can be performed. Conventionally, this is referred to as the G_0W_0 approximation. To improve upon this one-shot approach, the ev*GW* procedure can be used instead: QP energies are updated both in the calculation of the non-local, energy-dependent microscopic dielectric function determined within the RPA and in the Green's function until eigenvalue (ev) self-consistency is reached.

Neutral excitations with a conserved number of electrons and a change in their configuration S ($|N, 0\rangle \to |N, S\rangle$) rely instead on the two-particle Green's function.[19] This can be obtained from another Dyson-like equation of motion known as the Bethe–Salpeter Equation (BSE).[35] It determines the four-point density response function of the interacting system from the non-interacting system (see Refs. 15, 21, and 41 and references therein for a detailed derivation). In the specific case of optical excitations, one can employ a product basis of QP wave functions for coupled electron–hole amplitudes, i.e.,

$$\begin{aligned}\chi_S(\boldsymbol{r}_{\mathrm{e}}, \boldsymbol{r}_{\mathrm{h}}) = &\sum_{v}^{\mathrm{occ}}\sum_{c}^{\mathrm{unocc}}\sum_{\sigma\sigma'}A_{vc,\sigma\sigma'}^{S}\phi_{c,\sigma'}(\boldsymbol{r}_{\mathrm{e}})\phi_{v,\sigma}^{*}(\boldsymbol{r}_{\mathrm{h}})\\ &+ B_{vc,\sigma\sigma'}^{S}\phi_{v,\sigma'}(\boldsymbol{r}_{\mathrm{e}})\phi_{c,\sigma}^{*}(\boldsymbol{r}_{\mathrm{h}}),\end{aligned} \tag{8}$$

where $\boldsymbol{r}_{\mathrm{e}}$ ($\boldsymbol{r}_{\mathrm{h}}$) is for the electron (hole) coordinate, and we drop the label QP for clarity. Here, $A_{vc,\sigma\sigma'}$ ($B_{vc,\sigma\sigma'}$) are the expansion coefficients of the excited state wave function in terms of resonant (anti-resonant) transitions between QP occupied (occ.) states v and unoccupied (unocc.) c with spin σ and σ', respectively. With this choice of basis, the BSE can be transformed into an effective two-particle Hamiltonian problem of the form

$$\begin{pmatrix}\underline{\boldsymbol{H}}^{\mathrm{res}} & \underline{\boldsymbol{K}}\\ -\underline{\boldsymbol{K}} & -\underline{\boldsymbol{H}}^{\mathrm{res}}\end{pmatrix}\begin{pmatrix}\boldsymbol{A}^{S}\\ \boldsymbol{B}^{S}\end{pmatrix} = \Omega_S\begin{pmatrix}\boldsymbol{A}^{S}\\ \boldsymbol{B}^{S}\end{pmatrix}. \tag{9}$$

Assuming that spin–orbit coupling is negligible, this Hamiltonian has a block structure in terms of the spin combinations.[61] It can be decoupled into singlet and triplet Hamiltonians, allowing us to drop the explicit spin variables. Then, the matrix elements of $\underline{\boldsymbol{H}}^{\mathrm{res}}$ and $\underline{\boldsymbol{K}}$ are calculated as

$$H_{vc,v'c'}^{\mathrm{res}} = D_{vc,v'c'} + \kappa K_{vc,v'c'}^{\mathrm{x}} + K_{vc,v'c'}^{\mathrm{d}} \tag{10}$$

$$K_{cv,v'c'} = \kappa K_{cv,v'c'}^{\mathrm{x}} + K_{cv,v'c'}^{\mathrm{d}}, \tag{11}$$

where $\kappa = 2$ (0) for spin singlet (triplet) excitations and

$$D_{vc,v'c'} = (\varepsilon_c - \varepsilon_v)\delta_{vv'}\delta_{cc'}, \tag{12}$$

$$K_{vc,v'c'}^{\mathrm{x}} = \int \mathrm{d}^3\boldsymbol{r}_{\mathrm{e}}\,\mathrm{d}^3\boldsymbol{r}_{\mathrm{h}}\,\phi_c^{*}(\boldsymbol{r}_{\mathrm{e}})\phi_v(\boldsymbol{r}_{\mathrm{e}})v_{\mathrm{c}}(\boldsymbol{r}_{\mathrm{e}}, \boldsymbol{r}_{\mathrm{h}})\phi_{c'}(\boldsymbol{r}_{\mathrm{h}})\phi_{v'}^{*}(\boldsymbol{r}_{\mathrm{h}}), \tag{13}$$

$$K^{\mathrm{d}}_{vc,v'c'} = -\int \mathrm{d}^3\boldsymbol{r}_\mathrm{e}\,\mathrm{d}^3\boldsymbol{r}_\mathrm{h}\,\phi^*_c(\boldsymbol{r}_\mathrm{e})\phi_{c'}(\boldsymbol{r}_\mathrm{e})W(\boldsymbol{r}_\mathrm{e},\boldsymbol{r}_\mathrm{h},\omega=0)\phi_v(\boldsymbol{r}_\mathrm{h})\phi^*_{v'}(\boldsymbol{r}_\mathrm{h}). \tag{14}$$

The exchange interaction K^{x} originates from the bare interaction v_c and is responsible for the singlet–triplet splitting. The direct interaction K^{d} contains the attractive, but screened, interaction W between the electron and hole. This interaction is responsible for the binding of the electron–hole pair. Furthermore, it is assumed here that the dynamic properties of $W(\omega)$ are negligible and the computationally less demanding static approximation $\omega = 0$ is sufficient.

In systems for which the elements of the off-diagonal blocks $\underline{\boldsymbol{K}}$ in Eq. (9) are negligible, it is legitimate to use the Tamm–Dancoff Approximation (TDA)[62] in which the electron–hole amplitude is expressed as

$$\chi^{\mathrm{TDA}}_S(\boldsymbol{r}_\mathrm{e},\boldsymbol{r}_\mathrm{h}) = \sum_v^{\mathrm{occ}}\sum_c^{\mathrm{unocc}} A^S_{\mathrm{TDA},vc}\phi_c(\boldsymbol{r}_\mathrm{e})\phi^*_v(\boldsymbol{r}_\mathrm{h}), \tag{15}$$

i.e., by resonant transitions from occupied v to unoccupied c states only. The effective Hamiltonian reduces to the upper diagonal block of Eq. (9),

$$\underline{\boldsymbol{H}}^{\mathrm{res}}\boldsymbol{A}^S_{\mathrm{TDA}} = \Omega^{\mathrm{TDA}}_S\boldsymbol{A}^S_{\mathrm{TDA}}. \tag{16}$$

The TDA is known to reduce triplet instabilities.[63,64] On the other hand, the coupling between resonant and anti-resonant parts is significant, and its neglect can cause deviations of several 0.1 eV from results obtained with the full approach,[22] in particular, for small molecules.

III. TECHNICAL DETAILS AND IMPLEMENTATION

A. GW–BSE with Gaussian orbitals

VOTCA–XTP uses Gaussian-type orbitals (GTOs) $\varphi_\alpha(\boldsymbol{r}) = \varphi_{\{\ell,m_\ell,\gamma,I\}}(\boldsymbol{r}) = N_{\ell\gamma}Y_{\ell m_\ell}|\boldsymbol{r}-\boldsymbol{R}_I|^l\exp(-\gamma|\boldsymbol{r}-\boldsymbol{R}_I|^2)$ with decay constant γ centered around atom position $\boldsymbol{R}_I$, where $Y_{\ell m_\ell}$ are spherical harmonics with angular momentum number ℓ and magnetic quantum numbers m_ℓ, and $N_{\ell\gamma}$ is a normalization constant to expand the one- and two-point quantities involved in both DFT and GW–BSE steps. Specifically, the KS states in Eq. (1) are expressed using these basis functions in real space as

$$\phi^{\mathrm{KS}}_i(\boldsymbol{r}) = \sum_\alpha c^i_\alpha\varphi_\alpha(\boldsymbol{r}), \tag{17}$$

turning Eqs. (1), (6), and (9) into (generalized) eigenvalue problems in matrix form. See also the discussion about efficient solvers for the BSE in Sec. III E. VOTCA–XTP evaluates the integrals of the respective operators over the Gaussian basis functions using the modified recursive algorithms by Obara and Saika[65,66] for contracted Gaussian basis functions with $l \le 4$.

Of particular importance is the computation of 4-center repulsion integrals over the GTOs,

$$(\alpha\beta|\alpha'\beta') = \iint \mathrm{d}^3\boldsymbol{r}\,\mathrm{d}^3\boldsymbol{r}'\,\frac{\varphi_\alpha(\boldsymbol{r})\varphi_\beta(\boldsymbol{r})\varphi_{\alpha'}(\boldsymbol{r}')\varphi_{\beta'}(\boldsymbol{r}')}{|\boldsymbol{r}-\boldsymbol{r}'|}, \tag{18}$$

which scales with N_b^4 (with N_b being the number of basis functions) and occurs in the KS Hamiltonian term $\widehat{V}_\mathrm{H}$ and in the self-energy. The set of N_b^2 unique product functions $\varphi_\alpha(\boldsymbol{r})\varphi_\beta(\boldsymbol{r})$ can be approximated by a smaller auxiliary basis containing only $N_\mathrm{aux} = 3N_\mathrm{b}$ to $5N_\mathrm{b}$ functions ξ_μ. This reduces the scaling from N_b^4 to N_b^3 by rewriting the 4-center integrals as a combination of 3-center and 2-center repulsion integrals,[67]

$$(\alpha\beta|\alpha'\beta') \approx \sum_{\mu,\nu}(\alpha\beta|\mu)(\mu|\nu)^{-1}(\nu|\alpha'\beta'), \tag{19}$$

where $(\mu|\nu)^{-1}$ is an element of the inverse of the 2-center repulsion matrix,

$$(\mu|\nu) = \iint \mathrm{d}^3\boldsymbol{r}\,\mathrm{d}^3\boldsymbol{r}'\,\xi_\mu(\boldsymbol{r})\frac{1}{|\boldsymbol{r}-\boldsymbol{r}'|}\xi_\nu(\boldsymbol{r}'), \tag{20}$$

and $(\alpha\beta|\mu)$ is an element of the 3-center repulsion tensor,

$$(\alpha\beta|\mu) = \iint \mathrm{d}^3\boldsymbol{r}\,\mathrm{d}^3\boldsymbol{r}'\,\varphi_\alpha(\boldsymbol{r})\varphi_\beta(\boldsymbol{r})\frac{1}{|\boldsymbol{r}-\boldsymbol{r}'|}\xi_\mu(\boldsymbol{r}'). \tag{21}$$

The expression in Eq. (19) appears formally as the insertion of a resolution-of-identity (RI) with metric $(\nu|\mu)^{-1}$.

Within the RI approximation, the elements of the QP Hamiltonian in the basis of KS states contain $\Sigma_{mn}(E) = \langle\phi^{\mathrm{KS}}_m|\widehat{\Sigma}(E)|\phi^{\mathrm{KS}}_n\rangle$ [Eqs. (6) and (7)], which are determined as

$$\Sigma_{mn}(E) = \sum_{\mu,\nu}\sum_l I^{ml}_\mu I^{nl}_\nu\frac{\mathrm{i}}{2\pi}\int \mathrm{d}\omega\,\frac{e^{\mathrm{i}\omega\theta}\epsilon^{-1}_{\mu\nu}(\omega)}{E+\omega-\varepsilon_l\pm\mathrm{i}\eta}, \tag{22}$$

where the factor with $\theta\to 0^+$ ensures convergence of the integral and the imaginary perturbations $\pm\eta$ avoid singularities on the real axis, where the plus (minus) is taken when l is occupied (unoccupied). Furthermore,

$$I^{ml}_\mu = \sum_\nu(\mu|\nu)^{-1/2}\sum_{\alpha,\beta}c^m_\alpha c^l_\beta(\alpha\beta|\nu) = \sum_\nu(\mu|\nu)^{-1/2}M^{ml}_\nu \tag{23}$$

and

$$\epsilon_{\mu\nu}(\omega) = \delta_{\mu\nu} - 2\sum_m^{\mathrm{occ}}\sum_l^{\mathrm{unocc}} I^{ml}_\mu I^{ml}_\nu\left[\frac{1}{\omega-(\varepsilon_m-\varepsilon_l)+2\mathrm{i}\eta} - \frac{1}{\omega+(\varepsilon_m-\varepsilon_l)-2\mathrm{i}\eta}\right] \tag{24}$$

is called the dielectric matrix. In the G_0W_0 approach, we take the KS energies $\varepsilon_i = \varepsilon^{\mathrm{KS}}_i$, whereas in the ev$GW$ approach, we take the QP energies $\varepsilon_i = \varepsilon^{\mathrm{QP}}_i$. Currently, VOTCA–XTP pre-calculates all integrals at the start of the calculation and keeps I^{ml}_μ in memory.

B. Frequency dependence of the self-energy

The frequency integration, in Eq. (4), is one of the major difficulties in a GW calculation. Although it is possible to perform a numerical integration, this is likely unstable, since the integrand needs to be evaluated in regions in which it ill-behaves. VOTCA–XTP offers different alternatives for an approximate or exact integration, summarized in the following. We present three methods: the first one that is exact yet takes too much computational effort, the second one that is exact and is reduced in scaling, and the third one that is approximate yet very well-scaled.

In the GW approach, it is customary to separate the self-energy $\Sigma = \mathrm{i}GW$ into its bare exchange part $\Sigma_\mathrm{x} = \mathrm{i}Gv_\mathrm{c}$ and its correlation part

$\Sigma_c = iG\widetilde{W}$, where $\widetilde{W} = W - v_c$. In the following, several approaches to determine the correlation part of Eq. (22) are presented.

1. Fully analytical approach (FAA)

The integral in Eq. (22) can be evaluated analytically, yielding an exact expression of the correlation part of the self-energy. Its evaluation requires the calculation of the reducible polarizability $\widehat{P}$. We can express it in terms of an eigenvalue decomposition of the RPA Hamiltonian $\widehat{H}^{\mathrm{RPA}}$,

$$\widehat{P}(\omega) = [\widehat{H}^{\mathrm{RPA}} - \omega]^{-1} = \sum_S \frac{|\chi_S\rangle\langle\chi_S|}{\Omega_S - \omega}, \tag{25}$$

where the RPA Hamiltonian obeys a BSE as in Eq. (9) with $\kappa = -1$ and $K^{\mathrm{d}} = 0$ in Eqs. (10) and (11).

We can apply analytic continuation to the complex plane and contour deformation techniques to the convolution Eq. (4).[30,68] The resulting matrix entries of the correlation part of the self-energy are given by

$$\Sigma_{c,mn}(E) = 2\sum_{l,S} \frac{R^S_{ml}R^S_{nl}}{E - \varepsilon_l \pm (\Omega_S - i\eta)}, \tag{26}$$

where $\pm$ denotes + (−) for l occupied (unoccupied) and the factor 2 accounts for spin degeneracy. The residues R^S_{mn} are calculated as

$$R^S_{mn} = \sum_{\mu,\nu}\sum_{v}^{\mathrm{occ}}\sum_{c}^{\mathrm{unocc}} I^{mn}_{\mu} I^{vc}_{\nu}(A^S_{vc} + B^S_{vc}). \tag{27}$$

While this approach is analytically exact, it is not feasible for large systems as the diagonalization of $\widehat{H}^{\mathrm{RPA}}$ scales as N^6 in computational effort and N^4 in memory required.[21]

2. Contour deformation approach (CDA)

To avoid the computational bottleneck due to the scaling of the FAA, an alternative approach, also involving analytic continuation of the integral over the real axis from Eq. (22) to the complex plane and contour deformation techniques, can be employed. It yields a different rewriting, containing an integral over the imaginary axis and residual contributions. Since the new integral is very peaked around the origin when $E \approx \varepsilon_\ell$ for some ℓ, we add a Gaussian function inside the integral and subtract its integral value on the outside. We then can calculate the matrix entries $\Sigma_{c,mn} = \Sigma^{\mathrm{int}}_{c,mn}(E) + \Sigma^{\mathrm{res}}_{c,mn}(E)$, with the integral term

$$\Sigma^{\mathrm{int}}_{c,mn}(E) = \frac{1}{\pi}\sum_{\mu,\nu,l} I^{ml}_{\mu} I^{nl}_{\nu} \int \mathrm{d}\omega \, \frac{E - \varepsilon_l}{\omega^2 + (E - \varepsilon_l)^2} \times \left[\kappa_{\mu\nu}(0)\mathrm{e}^{-\alpha^2\omega^2} - \kappa_{\mu\nu}(i\omega)\right], \tag{28}$$

which can be numerically evaluated using a Gauss–Laguerre quadrature method, and the residual term

$$\Sigma^{\mathrm{res}}_{c,mn}(E) = \sum_{\mu,\nu,l} I^{ml}_{\mu} I^{nl}_{\nu}\left[\kappa_{\mu\nu}(E - \varepsilon_l \pm i\eta)\Theta_l(E) - \frac{1}{2}\kappa_{\mu\nu}(0)\mathrm{e}^{\alpha^2(E-\varepsilon_l)^2}\,\mathrm{sgn}(E - \varepsilon_l)\,\mathrm{erfc}(\alpha|E - \varepsilon_l|)\right]. \tag{29}$$

Here, $\underline{\boldsymbol{\kappa}} = \underline{\boldsymbol{\epsilon}}^{-1} - \underline{\boldsymbol{I}}$, and α is a Gaussian scaling parameter adaptive to the numerical model to be used.[69,70] Furthermore, l occupied $\Theta_l(E)$ is −1 if $E < \varepsilon_l$ and −1/2 if $E = \varepsilon_l$; for the l unoccupied case, it is 1 if $E > \varepsilon_l$ and 1/2 if $E = \varepsilon_l$. By design, the FAA is, in principle, the most exact one, since it is parameter-free except for the dependence on the basis set. However, the same results can already be achieved with the CDA using a moderately sized numerical integration grid for the Gauss–Laguerre quadrature, which reduces the scaling. This asset, however, may depend on the implementation, which is currently under progress for the CDA.

3. Plasmon-pole model (PPM)

Instead of a formally exact treatment of the frequency dependence, it can be approximated within a generalized plasmon-pole model (PPM).[71,72] The dielectric matrix can be expressed in terms of its eigenvalues $\lambda_{\mu'}$ and eigenvectors $\Phi_{\mu'}$ as

$$\epsilon_{\mu\nu}(\omega) = \sum_{\mu'} \Phi^{\mu}_{\mu'}(\omega)\,\lambda_{\mu'}(\omega)\,\Phi^{\nu}_{\mu'}(\omega). \tag{30}$$

In the PPM, eigenvectors are assumed to be frequency-independent, so only the eigenvalues $\lambda_{\mu'}$ depend on ω. In particular, this approximate dependence reads

$$\lambda^{-1}_{\mu'}(\omega) \approx 1 + \frac{z_{\mu'}\omega_{\mu'}}{2}\left[\frac{1}{\omega - (\omega_{\mu'} - i\eta)} - \frac{1}{\omega + (\omega_{\mu'} - i\eta)}\right]. \tag{31}$$

Here, $z_{\mu'}$ denotes the plasmon-pole weight and $\omega_{\mu'}$ denotes the plasmon-pole frequency. These two model parameters are found by fitting the plasmon-pole model to the exact dielectric function,[73] as shown in Eq. (24), for the frequencies $\omega = 0$ and $\omega = iE_0$, with E_0 being an additional model parameter, typically $E_0 = 0.5$ hartree. The correlation part of the self-energy results from the second term of Eq. (31), and its matrix entries are obtained as

$$\Sigma_{c,mn}(E) = 2\sum_{l,\mu'} \frac{1}{4}\frac{z_{\mu'}\omega_{\mu'} I^{ml}_{\mu'} I^{nl}_{\mu'}}{E - \varepsilon_l \pm \omega_{\mu'}}, \tag{32}$$

where $\pm$ denotes + (−) for l occupied (unoccupied) and the factor 2 accounts for spin.

4. Comparison of FAA and PPM for QP excitations of ethene and adenine

Figure 1 illustrates the influence of the choice of technique for the frequency integration on the obtained QP corrections to the KS state energies for two small molecules: ethene and adenine. In both cases, the calculations have been performed using the aug-cc-pVTZ basis,[74] an optimized RI basis,[75] and the PBE0[76] functional for the DFT ground-state calculation, with the whole range of states (121 for ethene and 399 of adenine) included in the RPA and QP steps. The corrections for all occupied levels and the same number of unoccupied levels are shown. Clearly, the QP corrections obtained with the PPM are slightly more positive (about 0.3 eV) than those with the exact method for the occupied and lowest unoccupied levels in both cases, whereas there is hardly any deviation for unoccupied levels at higher energy. It should be noted that, due to the nature of the deviations, energy differences near the gap are very similar for both methods. In particular, the QP gap between highest occupied molecular orbital (HOMO) and lowest occupied molecular orbital (LUMO) levels as predicted by the PPM and the exact method differs by only 0.05 eV for the two molecules considered here. It is also

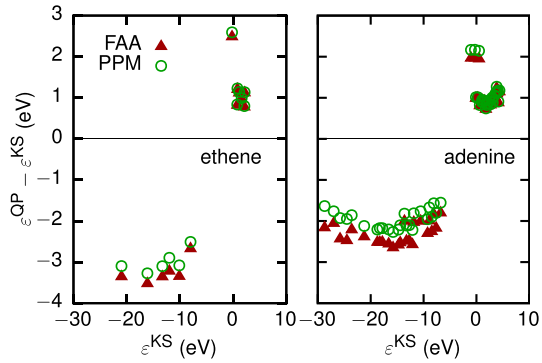

FIG. 1. Comparison of the QP corrections $\varepsilon^{QP} - \varepsilon^{KS}$ vs the KS energies for ethene (left) and adenine (right), obtained with the frequency integration of Eq. (4) using the FAA (triangles) and the PPM (circles), respectively.

visible that the corrections, e.g., to the DFT LUMO level in ethene, are larger than those for higher unoccupied states, leading to level switching in *GW* (LUMO+3). This behavior is the same for the FAA and PPM. However, this close agreement is paralleled by a significant difference in computational cost:[77] while the use of Eq. (26) increases the computation time from 4 min to 12 min compared to the PPM in ethene, we find that for adenine, the same causes an increase from 174 min to 2566 min.

Considering the above, we find that the PPM appears to be a suitable "low-cost" approximation to the exact frequency dependence of the self-energy when the main interest is in near-gap excitations such as HOMO and LUMO energies or HOMO–LUMO transitions in larger molecular systems. More significant deviations can be expected when mixed transitions involving other orbitals are investigated. We use the PPM for the showcase applications in Sec. IV.

C. Software development strategies

VOTCA–XTP is written in C++ and mostly adheres to the C++14 standard.[78] It can be obtained on www.github.com/votca/xtp. We use the Git feature branch workflow combined with code review and continuous integration, which executes code formatting, static analyzers, debug and release builds, and the test-suite. We use CMake as the build system, which also resolves the inclusion of external dependencies. The linear algebra is handled by Eigen,[79] which can be accelerated by internally calling the Intel Math Kernel Library.[80] For serialization, the HDF5 format is used via the canonical libraries.[81] Exchange-correlation functionals are provided by the Library of eXchange-Correlation (LIBXC) functionals.[82] Various boost packages[83] are used for file system string operations. Doxygen is used to document the APIs of VOTCA–XTP and automatically deploys to http://doc.votca.org.

VOTCA–XTP is designed as a library, which is linked to very thin executables, which can execute a variety of calculators by adding keywords on the command line. Virtual interfaces and factory patterns make the addition of new calculators simple. The same architecture is used for external DFT and MD codes, making VOTCA–XTP easily extensible. Lower-level data structures make use of template metaprogramming to support a variety of data types.

D. GPU acceleration

The computation of the $M_\nu^{ml} = \sum_{\alpha,\beta} c_\alpha^m c_\beta^l (\alpha\beta|\nu)$ term described in Eq. (23) requires the convolution of the 3-center repulsion tensor from Eq. (21) with the molecular orbital coefficients. These convolutions involve a large number of matrix–matrix multiplications that take a significant fraction of the computation time. In VOTCA–XTP, we have accelerated these operations by offloading them to a GPU, using the highly optimized CuBLAS library.[84] Moreover, due to the typically limited memory of the GPU and the latency required to copy the matrices back and forth from the device, there are limitations to the theoretical speedup for a given system size.

Table I illustrates the time trend for the calculation of 3-center integrals on a GPU (Nvidia Titan Xp) and single central processing unit (CPU) thread [Intel(R) Xeon(R) Gold 5120] as the molecular size increases. For systems smaller than benzene, the acceleration achieved by the GPU does not compensate for much of the communication latency, and consequently, the reduction in calculation time is limited, albeit on an already overall low level. For benzene and naphthalene, we observe a GPU speedup of about 60% compared to the respective single CPU thread values, while for the larger systems (phenanthrene and coronene), it increases to 80%. For even larger systems, the speedup increases until it eventually plateaus due to limits in the GPU memory and hardware bandwidth. Even though the observed quantitative speedups depend on the given GPU/CPU hardware combination, a qualitatively similar behavior is expected in a general setting. Note that overall, best performance is obtained by combining all CPU threads and the GPU in a mixed hybrid OpenMP/Cuda mode, which is also implemented in VOTCA–XTP.

E. Iterative matrix-free eigensolvers for the BSE

The size of the BSE matrix in Eq. (9) increases rapidly with the number of occupied (N_{occ}) and unoccupied (N_{unocc}) states included in the product basis, with its dimension being $2N_{BSE} \times 2N_{BSE}$, where $N_{BSE} = N_{occ} \times N_{unocc}$. Even if the TDA [Eq. (16)] is used, the dimension of $\underline{\boldsymbol{H}}^{res}$ is still $N_{BSE} \times N_{BSE}$. This leads to a computational as well as a memory bottleneck for *GW*–BSE calculations. The Davidson algorithms[85,86] form a family of subspace-iterative diagonalization schemes that are extensively used in large-scale quantum chemistry applications.[87,88] These methods allow rapid computation of a selected number of eigenvalues of large matrices, while reducing memory requirements when compared to other methods.

TABLE I. Comparison of calculation times for the convolution of the 3-center repulsion tensor with the molecular orbital coefficients on CPU [single thread of Intel(R) Xeon(R) Gold 5120] and GPU (Nvidia Titan Xp), respectively, for four polycyclic aromatic hydrocarbons with different numbers of functions in the basis (N_b) and auxiliary basis (N_{aux}).

			Time (s)	
Molecule	N_b	N_{aux}	CPU	GPU
Benzene	174	774	21	9
Naphthalene	274	1228	68	28
Phenanthrene	374	1682	216	44
Coronene	600	2724	1421	266

For an eigenproblem $\underline{\boldsymbol{H}}\boldsymbol{X} = \Omega\boldsymbol{X}$, the Davidson method starts from a set of N guess eigenvectors $\underline{\boldsymbol{V}} = \{\boldsymbol{v}_1, \boldsymbol{v}_2, \cdots, \boldsymbol{v}_N\}$, where each $\boldsymbol{v}_i$ is a column vector. These vectors are used to obtain a small eigenvalue problem,

$$(\underline{\boldsymbol{V}}^T \underline{\boldsymbol{H}}\,\underline{\boldsymbol{V}})\boldsymbol{x} = \omega\boldsymbol{x}. \tag{33}$$

The Ritz eigenpairs of this problem $(\omega_i, \boldsymbol{y}_i = \underline{\boldsymbol{V}}\boldsymbol{x}_i)$ are approximate solutions of the large eigenvalue problem. The residues of the Ritz eigenpairs, $\boldsymbol{r}_i = \underline{\boldsymbol{H}}\boldsymbol{y}_i - \omega_i\boldsymbol{y}_i$, are then used to construct additional basis vectors, $\boldsymbol{t}_i$, which are appended to the projector, $\underline{\boldsymbol{V}} = \{\boldsymbol{v}_1, \boldsymbol{v}_2, \cdots, \boldsymbol{v}_N, \boldsymbol{t}_1, \boldsymbol{t}_2, \cdots, \boldsymbol{t}_n\}$. This new projector is then orthogonalized, using either a Gram–Schmidt or a QR approach and used to obtain a better approximation of the large eigenpairs. This is repeated until the residues of all Ritz eigenpairs follow the condition $\|\boldsymbol{r}_i\| \leq \epsilon$, where ϵ is a fixed threshold parameter. When the size of the projector $\underline{\boldsymbol{V}}$ becomes too large, it is reset to N Ritz eigenvectors.

In addition to considerably accelerating the diagonalization of the BSE matrix, these methods do not require the matrix to be stored in memory and only the action of this matrix on vectors is required. This matrix-free approach naturally decreases the memory requirement of the calculation. Different methods based on the general idea behind the Davidson algorithm have been developed. These methods differ in the way the correction vectors $\boldsymbol{t}_i$ are calculated and on which part of the spectrum is targeted. We briefly present the solutions we have implemented in VOTCA–XTP to solve the BSE equation using the TDA or the full matrix.

If the TDA is used, the Davidson method allows rapid computation of the lowest N eigenvalues and eigenvectors of the Hermitian matrix $\underline{\boldsymbol{H}}^{\text{res}}$. The initial projector $\underline{\boldsymbol{V}}$ is then set to select the N transitions with the lowest energy difference. We have implemented different methods to compute the correction vectors. Following Davidson's original idea,[85] the correction vectors can be obtained via

$$\boldsymbol{t}_i = -(\underline{\boldsymbol{D}}^{\text{res}} - \omega_i\underline{\boldsymbol{I}})^{-1}\boldsymbol{r}_i, \tag{34}$$

where $\underline{\boldsymbol{D}}^{\text{res}}$ is the diagonal of the matrix $\underline{\boldsymbol{H}}^{\text{res}}$. Note that $(\underline{\boldsymbol{D}}^{\text{res}} - \omega_i\underline{\boldsymbol{I}})$ is a diagonal matrix and that therefore, it is not necessary to explicitly diagonalize it. It is important to mention that the method outlined above requires only one evaluation of $\underline{\boldsymbol{H}}^{\text{res}}\underline{\boldsymbol{V}}$ per iteration. This product can be calculated without having to form the complete $\underline{\boldsymbol{H}}^{\text{res}}$ matrix, decreasing the memory requirement at the expense of a slight increase in computational time.

If the TDA is not used, the lowest transitions correspond to the interior eigenvalues of the non-Hermitian matrix in Eq. (9), as all its eigenvalues come in pairs $(-\Omega_S, \Omega_S)$. The procedure outlined above is optimal for exterior eigenvalues but often leads to spurious eigenvalues when applied to the calculation of interior eigenvalues. Following Morgan,[89] the original Rayleigh–Ritz approach is modified to map the interior eigenvalues to the exterior of the spectrum of an inverted matrix. To this end, the small eigenvalue problem Eq. (33) is replaced by the generalized eigenvalue problem,

$$(\underline{\boldsymbol{V}}^T\underline{\boldsymbol{H}}\underline{\boldsymbol{V}})\boldsymbol{x} = \omega(\underline{\boldsymbol{V}}^T\underline{\boldsymbol{H}}^2\underline{\boldsymbol{V}})\boldsymbol{x}. \tag{35}$$

Solving Eq. (35) gives the harmonic Ritz eigenpairs $(\omega_i, \boldsymbol{y}_i = \underline{\boldsymbol{V}}\boldsymbol{x}_i)$ with $\omega_i = \boldsymbol{x}_i^T\underline{\boldsymbol{V}}^T\underline{\boldsymbol{H}}\underline{\boldsymbol{V}}\boldsymbol{x}_i$. As mentioned before, the residues of these eigenpairs are used to construct correction vectors using Eq. (34), which are then appended to the projector matrix $\underline{\boldsymbol{V}}$. It is worth noting that the generalized eigenvalue problem Eq. (35) requires two matrix-vector products per iteration to evaluate $\underline{\boldsymbol{H}}\underline{\boldsymbol{V}}$ and $\underline{\boldsymbol{H}}^2\underline{\boldsymbol{V}}$, which significantly increases the computational cost of the method.

To illustrate the performance of our implementation of the Davidson algorithm, we show in Table II the computation time and the memory requirement of the BSE calculations of four nucleobases. Here, the Davidson method [Diagonal-Preconditioned-Residue (DPR)] using Eq. (34) to obtain the correction vectors and its matrix-free implementation (DPR-MF) are compared to the highly optimized Lapack routine DSYVEX, which also allows the calculation of the lowest part of the spectrum. As shown in Table II, the DPR method is up to 2 orders of magnitude faster than DSYVEX, while having similar memory requirements. The matrix-free approach is faster than DSYVEX, but significantly reduces the memory requirement, hence enabling BSE calculations on much larger systems. The speed-up offered by the Davidson method over DSYVEX is most apparent when only a small number of eigenvalues are required. For example, in the case of the adenine molecule, the calculations of the lowest 1000 eigenvalues of the BSE matrix required approximately the same amount of time using the DPR or DSYVEX methods, while the DPR-MF was twice as slow. Note that the full diagonalization of the BSE matrix is not supported by VOTCA–XTP due to the high computational cost and memory load that it would require. As a consequence, VOTCA–XTP is not suitable for computing the absorption spectrum of large systems far from the band edge.

TABLE II. Performance benchmark (computation time and memory requirements) of different diagonalization schemes implemented in VOTCA-XTP during the calculation of the 25 lowest singlet excitations of the $N_{\text{BSE}} \times N_{\text{BSE}}$ BSE matrices using the TDA on a single thread.

		Time (s)			Memory (GB)		
Molecule	N_{BSE}	DSYVEX	DPR	DPR-MF	DSYVEX	DPR	DPR-MF
Uracil	7 743	83.44	1.33	32.63	1.08	1.20	0.71
Cytosine	8 149	98.68	1.52	33.16	1.21	1.31	0.79
Thymine	10 593	217.85	2.03	61.99	1.88	2.02	1.16
Adenine	11 725	293.49	2.39	75.48	2.18	2.38	1.28

F. QM/MM embedding schemes for QP and electron–hole excitations

As mentioned in Sec. I, VOTCA–XTP provides a coupled QM/MM framework in which the quantum (excited) state is linked to a polarizable atomistic model for the environment. Our scheme makes use of a distributed atomic multipole representation for molecules in the MM region, which allows treatment of both the effects of static electric fields and the polarization response as a self-consistent reaction field. Specifically, static atomic multipole moments[90] Q_t^m are employed, where t indicates the multipole rank and m is the associated atom in the molecule M. The tensor $T_{tu}^{mm'}$ describes the interactions between the multipoles moments Q_t^m and $Q_u^{m'}$. To model the polarization effects, each atom can be additionally assigned a polarizability $\alpha_{tu}^{mm'}$ for the creation of induced moments ΔQ_t^m due to the field generated by moments u on a different atom m'. If we split a classical MM system $\mathcal{S}$ in state s into regions $\mathcal{R}$ and $\mathcal{R}'$ with $\mathcal{S} = \mathcal{R} \cup \mathcal{R}'$, its total energy is given by

$$E_{\text{class}}^{(s)}(\mathcal{S}) = E^{(s)}(\mathcal{R}) + E^{(s)}(\mathcal{R}') + E^{(s)}(\mathcal{R}, \mathcal{R}'), \tag{36}$$

where

$$E^{(s)}(\mathcal{R}) = \frac{1}{2} \sum_{M \in \mathcal{R}} \sum_{\substack{M' \in \mathcal{R} \\ M' \neq M}} E_{MM'}^{(s)} + \frac{1}{2} \sum_{M \in \mathcal{R}} E_M^{(s)}, \tag{37}$$

$$E^{(s)}(\mathcal{R}, \mathcal{R}') = \sum_{M \in \mathcal{R}} \sum_{M' \in \mathcal{R}'} E_{MM'}^{(s)}, \tag{38}$$

with

$$E_{MM'}^{(s)} = \sum_{m \in M} \sum_{m' \in M'} \sum_{tu} (Q_t^{m(s)} + \Delta Q_t^{m(s)}) T_{tu}^{mm'} (Q_u^{m'(s)} + \Delta Q_u^{m'(s)}) \tag{39}$$

and

$$E_M^{(s)} = \sum_{m \in M} \sum_{\substack{m' \in M \\ m' \neq m}} \sum_{tu} \Delta Q_t^{m(s)} (\alpha^{-1})_{tu(s)}^{mm'} \Delta Q_u^{m'(s)}. \tag{40}$$

Equation (36) follows a variational principle with respect to the induced moments, and a preconditioned conjugate gradient method is used to find the ΔQ_t^m, which give the minimum energy. Induced interactions are modified using Thole's damping functions[91,92] to avoid overpolarization. Then, the MM multipoles can interact with the QM region as an additional external potential to Eq. (1), while the explicit electrostatic field from the QM density is used to polarize the MM region. In the GW–BSE framework, the density depends on the state of interest (s). If s is a quasiparticle excitation, we define

$$\rho_{\text{QP}}^{(s)}(\boldsymbol{r}) = \rho_{\text{DFT}}(\boldsymbol{r}) + f_s |\phi_s^{\text{QP}}(\boldsymbol{r})|^2, \tag{41}$$

with $f_s = -1$ for occupied and $f_s = +1$ for unoccupied QPs. If s is an electron–hole excitation, its total density is evaluated as

$$\rho^{(s)}(\boldsymbol{r}) = \rho_{\text{DFT}}(\boldsymbol{r}) + \rho_e^{(s)}(\boldsymbol{r}) - \rho_h^{(s)}(\boldsymbol{r}). \tag{42}$$

Here, the electron (hole) contribution of the exciton to the density is computed by integrating the squared excited-state wave function χ^S with respect to the hole (electron) coordinates, i.e.,

$$\begin{aligned} \rho_{\text{e}}^{(s)}(\boldsymbol{r}) &= \rho_{\text{e}}^{(s)}(\boldsymbol{r}_{\text{e}}) = \int d\boldsymbol{r}_{\text{h}} |\chi_S(\boldsymbol{r}_{\text{e}}, \boldsymbol{r}_{\text{h}})|^2, \\ \rho_{\text{h}}^{(s)}(\boldsymbol{r}) &= \rho_{\text{h}}^{(s)}(\boldsymbol{r}_{\text{h}}) = \int d\boldsymbol{r}_{\text{e}} |\chi_S(\boldsymbol{r}_{\text{e}}, \boldsymbol{r}_{\text{h}})|^2. \end{aligned} \tag{43}$$

More specifically, VOTCA–XTP can partition a system into multiple active QM regions (possibly treated at different levels of theory) and multiple classical MM regions in which static and polarizable multipoles of different orders can be defined, generalizing Eq. (36). In order to evaluate excitation energies within this QM/MM scheme, a self-consistent procedure is required if polarization is included in the MM region. Within a single iteration step p, a QM level calculation (DFT for the ground state $s = n$ and DFT +GW–BSE for electron–hole excited $s = x$ states) is performed in the electric field generated by the total moments in the MM region. The resulting QM energy then reads

$$E_{\text{QM}}^{(s),p} = E_{\text{DFT}}^{(s),p} + \delta_{sx} \Omega_S^p. \tag{44}$$

The associated total electron density is then evaluated on a grid. In VOTCA–XTP, the default quadrature on a grid used for the numerical integration is an Euler–MacLaurin scheme for the radial components and a Lebedev scheme for the angular components, and the discretized density is then used to self-consistently determine new induced dipoles in the MM region. The minimized classical energy $E_{\text{class}}^{(s),p}$ is used to update the total energy of the coupled QM/MM system,

$$E_{\text{QM/MM}}^{(s),p} = E_{\text{QM}}^{(s),p} + E_{\text{class}}^{(s),p}. \tag{45}$$

The whole procedure is repeated until the change in total energy is lesser than a preselected accuracy, typically 10^{-5} hartree.

To obtain the excitation energy $\Omega^{(s)}$ of a complex in the polarizable environment, total energies of the combined QM/MM system are obtained self-consistently for both the ground and excited state and their difference is defined as

$$\Omega^{(s)} = E_{\text{QM/MM}}^{(s)} - E_{\text{QM/MM}}^{(n)}. \tag{46}$$

An equivalent formulation for quasiparticle excitation energies uses the respective ε^{QP} instead of Ω_S in Eq. (44).

The above QM/MM procedures rely on the representation of the molecules in the MM region by static atomic multipoles and polarizabilities. These can be taken from standard parameterizations available, for instance, from the AMOEBA force field.[93] However, in many cases, it is necessary to make custom parameterizations. VOTCA–XTP can either read fitted partial charges from one of the supported external DFT packages or obtain them with its internal CHELPG[94] module. Higher order static multipoles can be taken from the Gaussian Distributed Multipole Analysis (GDMA) software.[95] VOTCA–XTP also provides a tool for the optimization of atomic polarizabilities after the static moments are defined. Starting from generic element-specific polarizabilities from AMOEBA, these are scaled atom-specific to reproduce the polarizable volume of the molecule as obtained from DFT.

IV. SHOWCASE APPLICATIONS

In this section, we demonstrate the application of VOTCA–XTP in two showcases related to materials used in organic photovoltaics. First, we investigate the optical excitation energies in a

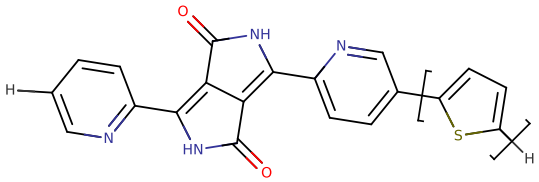

FIG. 2. Chemical structure of a monomer (n = 1) building block of the n-DPP2PymT oligomers with m = 1, 2, 3.

series of diketopyrrolopyrrole-derived oligomers. Second, we study the effects of donor–acceptor complex conformations and environment polarization on the CT excitations in a low-donor content blend of rubrene and fullerene.

A. Optical excitations of diketopyrrolopyrrole-derived oligomers

As a first showcase application, we investigate the excited-state properties of a series of diketopyrrolopyrrole (DPP) oligomers as model systems for the respective polymers. The chemical structure of the monomer building blocks is shown in Fig. 2. We consider structural variants containing m = 1, 2, 3 thiophene rings (in *trans* orientation) in the monomer unit, as well as oligomers consisting of up to n = 4 repeat units, further referred to as n-DPP2PymT. This choice not only allows us to study the physical system but also enables us to simultaneously highlight the systematic increase in size of the computational system and the associated powers and limitations of the current implementation. In its ground state, the DPP core is highly electron-withdrawing. Hence, nucleophilic aromatic substituents are added to the DPP core.[53] In the compounds studied, pyridine is used as an aromatic substituent, which lowers the highest occupied molecular orbital (HOMO) and the lowest occupied molecular orbital (LUMO) levels due to the presence of sp^2-hybridized nitrogen.[54] Further addition of thiophene (a stronger nucleophile) increases the number of aromatic substituents in conjugation with DPP. The donor strength increases consequently as evident from the HOMO energy levels determined by cyclic voltammetry measurements.[55] This addition of thiophene also minimally influences the LUMO, and the optical excitation energy is lowered from 2.22 eV for m = 1 to 2.05 eV for m = 3.[55]

Geometry optimizations for the n-DPP2PymT oligomers have been carried out within DFT based on the cc-pVTZ basis set[75] with the PBE0 hybrid functional[76] using the ORCA package.[44] Initial structures for all oligomers have been prepared as suggested by experiments with the thiophenes in *trans* orientation to each other, and the final obtained geometries are nearly planar.

For the subsequent GW–BSE calculations, we chose the evGW approach with the PPM. An optimized auxiliary basis set for cc-pVTZ[74] taken from the Basis Set Exchange[96] has been used in the resolution-of-identity steps. Aiming at a consistent benchmark, we use in each case the full spectrum of single-particle states in the RPA (N_{RPA}) and determine QP corrections to all occupied (N_{occ}) and $N_{\mathrm{unocc}} = 2N_{\mathrm{occ}}$ unoccupied states. The latter are also taken into account in the product basis for the BSE, i.e., $N_{\mathrm{BSE}} = N_{\mathrm{occ}} \cdot N_{\mathrm{unocc}}$. The explicit values as listed in Table III for all oligomers. Due to computational limitations, only systems with n = 1, 2, 3 could be treated for n-DPP2Py3T. The HOMO and LUMO energies as

TABLE III. Number of RPA levels (N_{RPA}), number of occupied (N_{occ}) and unoccupied levels ($N_{\mathrm{unocc}} = 2N_{\mathrm{occ}}$), the product basis set size for BSE calculations (N_{BSE}), Kohn–Sham HOMO ($\varepsilon^{\mathrm{KS}}_{\mathrm{HOMO}}$) and LUMO ($\varepsilon^{\mathrm{KS}}_{\mathrm{LUMO}}$) energies, quasi-particle HOMO ($\varepsilon^{\mathrm{QP}}_{\mathrm{HOMO}}$) and LUMO ($\varepsilon^{\mathrm{QP}}_{\mathrm{LUMO}}$) energies, and optical excitation energies for TDA ($\Omega^{\mathrm{TDA}}_{\mathrm{opt}}$) and full BSE ($\Omega^{\mathrm{full}}_{\mathrm{opt}}$) for the n-DPP2PymT oligomers. All energies are given in eV.

	N_{RPA}	N_{occ}	N_{unocc}	N_{BSE}	$\varepsilon^{\mathrm{KS}}_{\mathrm{HOMO}}$	$\varepsilon^{\mathrm{KS}}_{\mathrm{LUMO}}$	$\varepsilon^{\mathrm{QP}}_{\mathrm{HOMO}}$	$\varepsilon^{\mathrm{QP}}_{\mathrm{LUMO}}$	$\Omega^{\mathrm{TDA}}_{\mathrm{opt}}$	$\Omega^{\mathrm{full}}_{\mathrm{opt}}$
1-DPP2Py1T	982	96	191	18 336	−5.73	−2.93	−6.76	−1.31	2.79	2.44
2-DPP2Py1T	1935	191	381	72 771	−5.66	−3.19	−6.57	−1.73	2.45	2.22
3-DPP2Py1T[a]	2890	286	571	163 306	−5.65	−3.30	−6.52	−1.90	2.31	2.11
4-DPP2Py1T[a]	3844	381	761	289 941	−5.64	−3.36	−6.50	−1.97	2.25	2.06
Expt.[b]							−6.05	−3.83		1.81
1-DPP2Py2T	1164	117	233	27 261	−5.64	−2.95	−6.65	−1.39	2.68	2.38
2-DPP2Py2T	2300	233	465	108 345	−5.55	−3.15	−6.42	−1.73	2.35	2.15
3-DPP2Py2T[a]	3436	349	697	243 253	−5.53	−3.23	−6.38	−1.84	2.25	2.07
4-DPP2Py2T[c]	4572	465	929	431 985	−5.53	−3.26	−6.36	−1.90	2.19	2.03
Expt.[b]							−5.96	−3.80		1.73
1-DPP2Py3T	1346	138	275	37 950	−5.55	−2.96	−6.53	−1.45	2.60	2.34
2-DPP2Py3T	2664	275	549	150 975	−5.46	−3.11	−6.32	−1.72	2.29	2.11
3-DPP2Py3T[a]	3982	412	823	339 076	−5.45	−3.17	−6.28	−1.81	2.20	2.05
Expt.[b]							−5.77	−3.72		1.74

[a]Needs more than 256 GB RAM.
[b]From Ref. 55. Measurements of HOMO/LUMO performed with cyclic voltammetry of thin films, absorption data from dilute solution in chloroform. In both cases, polymers with different bulky, branched alkyl side chains are used.
[c]Needs more than 512 GB RAM.

obtained in the KS and QP approaches and the optical excitation energies resulting from the TDA and the full BSE are also given in Table III.

The quasi-particle energies for HOMO and LUMO follow the expected trend with the increasing number of thiophene units m, as discussed above. We observe that for all oligomers, increasing the number of repeat units n initially, i.e., from monomer to dimer, affects the HOMO energies by about 0.2 eV. Upon further additions of repeat units, the values tend to saturate, indicating that the electronic excitations remain localized. Table III also includes experimental values for the HOMO and LUMO levels of polymers of the three respective structures, as determined by cyclic voltammetry measurements in thin films.[55] The *GW* calculated and experimentally observed $\varepsilon^{\mathrm{QP}}$ values are found to demonstrate the same behavior as the experiment with the increasing number of thiophenes. Quantitative differences can be attributed to the lack of environment effects in the vacuum calculations.[48]

A similar trend is apparent for the energy of the optically active singlet excitations, as shown in Fig. 3, for calculations based on the full BSE (solid lines) and using the TDA (dashed lines), respectively. The values for $\Omega_{\mathrm{opt}}^{\mathrm{full}}$ obtained for the largest systems are close to those obtained in solution[55] (1.81 eV for DPP2Py1T, 1.73 eV in DPP2Py2T, and 1.74 eV in DPP2Py3T). It is also noteworthy that even for the biggest oligomers, the difference between the TDA and the full BSE is about 0.2 eV. This is a further indication of the fact that the electronic states and excitations do not delocalize completely over the whole oligomer but remain localized on a few repeat units.[26]

This notion is corroborated by the visualizations of the electron density difference upon excitation, as shown by insets in Fig. 3. Although the DPP bicyclic core is electron withdrawing, upon exciton generation, the electron density is reduced there. In the case of 1-DPP2Py1T, the change in electronic density is visible over the entire small molecule. In contrast, for 4-DPP2Py1T, we note that

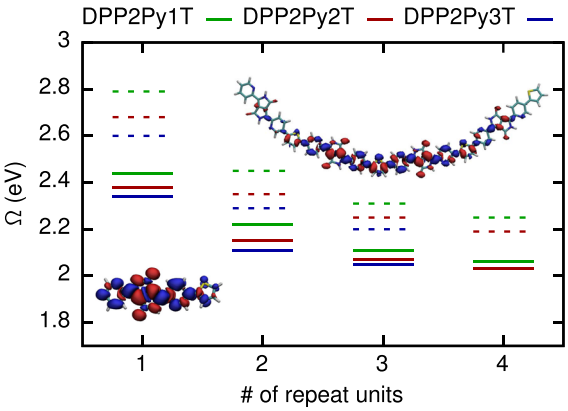

FIG. 3. Excitation energy Ω (in eV) for the DPP2PymT oligomers as a function of the number of repeat units. The solid lines represent the energies obtained using the full BSE, while the respective dashed ones result from the TDA. The increased electron density and increased hole density (isovalue $\pm 2 \cdot 10^{-4}\, e/a_B^3$) are shown in blue and red, respectively, after exciton formation. The molecules shown are 4-DPP2PyT (top) and 1-DPP2PyT (bottom).

the termini of the oligomer are nearly free of either hole or electron density, with the excitation appearing to be localized on about three repeat units.

Turning now toward the computational effort required to obtain these results, we first observe that, as also noted in Table III, systems with up to roughly $N_b = 2500$ basis functions (the same as N_{RPA}) can be treated on machines with less than 256 GB of memory. More than 512 GB are needed for the biggest oligomer (4-DPP2Py2T). These requirements can be considered typical for most organic compounds with similar composition and arise from the aforementioned storage of the three-center integrals I_μ^{ml} [Eq. (23)] in memory (see Sec. III A) containing $(N_{\mathrm{occ}} + N_{\mathrm{unocc}}) \cdot N_{\mathrm{RPA}} \cdot N_{\mathrm{aux}}$ doubles. It should be emphasized that this apparent limitation of the system sizes accessible on regular workstations can be overcome by choosing a lower N_{RPA}, fewer states in the QP and BSE steps, or a smaller basis set than the large cc-pVTZ set used here for demonstration purposes.[41] We also stress that the peak memory required is reached in the RPA of the *GW* step, and obtaining the solution of the BSE does not increase it as we make use of the matrix-free Davidson (DPR-MF) method, as introduced in Sec. III E.

B. Molecular and charge-transfer excitations in rubrene–fullerene mixtures

The second application example showcases VOTCA–XTP's capability to determine the different excited states of molecular complexes within the *GW*–BSE/MM embedding schemes. Here, we focus on representative structures of a donor–acceptor heterojunction as used in organic photovoltaics. In particular, we study an amorphous morphology with low-donor content (<10 mol. %), composed of fullerene (C_{60}) and 5,6,11,12-tetraphenyltetracene (rubrene). Because of the low-donor content, aC_{60} cluster will surround the donor molecule, making the interaction between the single donor molecule and a close shell of neighboring C_{60} acceptors representative of the properties of the system as a whole. These complexes are therefore meaningful candidates for a computational analysis of the influence of donor–acceptor conformations and environment polarization effects in the *GW*–BSE/MM framework introduced in Sec. III F.

To obtain representative structures, mixed morphologies have been simulated with *ab initio* MD based on density functional tight binding theory using linear scaling self consistent field calculations within the CP2K code.[97] Initial configurations have been prepared using packmol,[98] targeting experimental values[56] for densities and mole percentages. This structure is first equilibrated at 700 K in *NpT* (with velocity rescaling thermostat[99] at atmospheric pressure[100]) for 7 ps (time step 1 fs) and then annealed to 300 K within 10 ps. A final *NpT* equilibration followed for 5 ps.

In the final morphology, donor–acceptor complexes with many different orientations between fullerene and rubrene molecules are present, and we focus here on the two cases shown in Fig. 4. The first configuration, labeled CT_P, displays a center-of-mass distance of $\Delta_{\mathrm{COM}} = 11.3$ Å between the two molecules, and their closest contact distance $\Delta_{\mathrm{CC}} = 3.3$ Å is found between a carbon atom in C_{60} and a hydrogen atom of one phenyl group in rubrene. On the other hand in the CT_A configuration, the two molecules are closer ($\Delta_{\mathrm{COM}} = 8.9$ Å) and $\Delta_{\mathrm{CC}} = 1.8$ Å is found with respect to an atom in the anthracene core of rubrene. Such variations of the

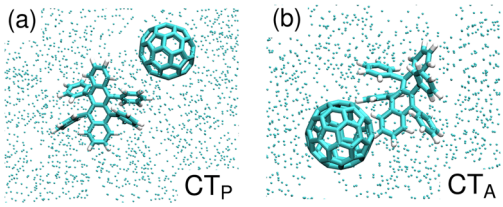

FIG. 4. View of the two rubrene–C_{60} configurations taken from the MD simulation. The QM complexes are surrounded by the MM atomic sites, here pictured as small spheres. In (a), the C_{60} is closer to one of the phenyl ring of rubrene, and this complex is referred to as CT_P. In the CT_A configuration (b), the fullerene is close to the anthracene core.

mutual orientations of rubrene and C_{60} in the two complexes are also expected to give rise to distinctly different characteristics of electronic excitations, intermolecular charge-transfer excitations above all.

For both configurations, we apply the *GW*–BSE/MM method described in Sec. III F. To keep the computational costs tractable, the calculations make use of effective core potentials and an associated basis set[101] that has been augmented by a single shell of polarization functions taken from the 6-311G** basis.[102] An associated auxiliary basis was constructed using the technique employed in the Symmetry-Adapted Perturbation Theory (SAPT) code.[103] The PBE0[76] functional has been used for the underlying DFT ground-state calculations. In the *GW*–BSE steps, a total of $N_{RPA} = 2366$ levels have been included in the RPA, and QP corrections have been determined for $N_{occ} = 218$ occupied and $N_{unocc} = 435$ unoccupied states. The corresponding product basis for the BSE in TDA is of size $N_{BSE} = 94\,830$. In the following, we determine the electron–hole excitations of the complexes in three embedding variants: in the gas-phase (vacuum, *GW*–BSE), in a static environment in which no polarization effects are included in the MM region within a cut-off of 2.2 nm (*GW*–BSE/MM$_s$), and in a polarizable environment (*GW*–BSE/MM$_p$), respectively.

The resulting excitation energies are shown in Fig. 5. In all cases, local excitations on C_{60} (rubrene) are marked in green (blue) and excitations with CT character are given by varying shades of red depending on the amount of charge transfer ΔQ. Note that in the case of *GW*–BSE/MM and *GW*–BSE/MM$_s$, one obtains the full spectrum of excitations from a single calculation. Due to the state-dependent response of the system in the polarizable case—requiring the self-consistent procedure as described in Sec. III F—only the lowest energy excitations with the respective characters are shown for *GW*–BSE/MM$_p$.

For both configurations, the spectra are hardly affected by the embedding in a static environment. This is due to the fact that most of the environment of the complexes is formed by C_{60} molecules, which only exhibit a faint electrostatic potential.

For the CT_P configuration [Fig. 5(a)], the lowest 15 excitations, as obtained by *GW*–BSE/MM$_s$, are localized on C_{60}, with the optically active rubrene excitation found right above them at about 2.4 eV. Charge-transfer excitations (with $\Delta Q = 1$, see also the isosurface plot in the inset) result another 0.2 eV higher in energy. Polarization as taken into account in the *GW*–BSE/MM$_p$ calculations has very little effect on the two localized excitations since both C_{60} and rubrene exhibit only a small change in molecular dipole moment upon excitation. In contrast, the creation of a CT exciton causes a large change in dipole moment to which the environment strongly responds. The electron–hole pair is also less strongly bound in the CT exciton and, therefore, itself more susceptible to changes in the environment. In total, this results in a strong energetic stabilization around 0.46 eV so that the CT state energy is found 0.24 eV below the rubrene excitation. This is qualitatively different to the situation observed without the inclusion of polarization effects, indicating that the formation of the CT state could be exothermic rather than endothermic.

The spectra of the CT_A are significantly different. In a vacuum or static environment, the three lowest excitations between 1.6 eV and 1.8 eV show partial charge transfer ($\Delta Q = 0.38$) due to a delocalization of the single-particle HOMO level over both molecules. Between 2.0 eV and 2.4 eV, the spectra are generally dense with excitations of different character being energetically close. The localized excitations result at very similar energies as in CT_P in the *GW*–BSE/MM$_p$ calculation. Similarly, also the energy of the CT excitation is only lowered by 0.03 eV, which we attribute to a combination of smaller dipole moment and lower polarizability of the excited state as compared to the one in CT_P. It is noteworthy, however, that the amount of charge transferred is increased to $\Delta Q = 0.68$. The non-integer type of CT can also be seen from the isosurface plot in the inset of Fig. 5(b) in which part of the hole density (red) is present on C_{60}. Conversion to CT excitations appears energetically favorable from both types of localized excitations in CT_A.

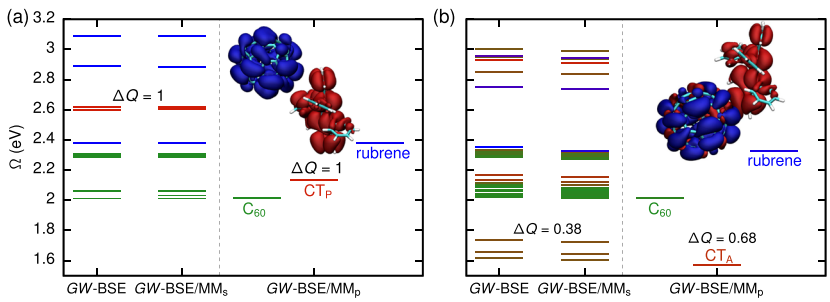

FIG. 5. Excitation energies Ω (in eV) as obtained for the CT_P (a) and CT_A (b) complexes from the *GW*–BSE calculations in vacuum and embedded in a static (*GW*–BSE/MM$_s$) and polarizable (*GW*–BSE/MM$_p$) environment, respectively. Local excitations on C_{60} (rubrene) are marked in green (blue) and excitations with CT character are given by varying shades of red depending on the amount of charge transfer ΔQ. Isosurfaces of the electron–hole densities with isovalue $\pm 10^{-4}\ e/a_B^3$ are shown as insets.

V. DISCUSSION

The two examples discussed in Sec. IV emphatically demonstrated the capabilities of VOTCA–XTP in calculating the excited-state electronic structure of molecular materials based on *GW*–BSE both in isolated molecular systems and in complex molecular aggregates. Our implementation is particularly suited for the study of near-gap excitations and performs well on regular workstations. There are, however, as briefly already discussed, some limitations, e.g., in terms of accessible system sizes, or ultimate accuracy depending on the method used for the frequency integration of the self energy.

All in all, the design of VOTCA–XTP aims at striking a balance between performance, accuracy, and implementation complexity. For instance, the RI approximation simplifies the implementation and speeds up the calculations. In particular, the N_b^3 scaling of the memory requirements of the RPA makes the storage of the three-center integrals in memory feasible for moderate-sized molecules described by up to approximately 1500 basis functions, thus allowing *GW*–BSE calculations even on desktop hardware. As VOTCA–XTP is built with shared memory parallelization, large memory hardware is required for the treatment of larger systems. This could, in principle, be overcome either by calculating the necessary terms on the fly or by efficiently storing them on a disk. Both would come with a notable drop in performance and are currently not actively pursued. Instead, we consider as an alternative the inclusion of a framework for Density Functional Perturbation Theory[104] (DFPT) into VOTCA–XTP. It has been shown before[105] that the explicit summation over unoccupied states in the RPA can be omitted, if the whole *GW* is rephrased in terms of a Sternheimer equation. In the same spirit, DFPT can also yield beneficial improvements in terms of speed and memory consumption for the BSE.[106]

Besides the above limitations, the *GW*–BSE implementation in VOTCA–XTP currently supports only closed-shell calculations, and thus, systems with explicit spin, e.g., for the optical spectra of cations or anions, cannot be treated. This restriction is planned to be lifted in future versions. Furthermore, VOTCA–XTP can only determine excited-state response properties such as atomic forces, excited-state vibrational modes, or polarization tensors via numerical derivatives due to the lack of analytic gradient expressions.[107] It is also known that while the GTO-based implementation is adequate for the representation of bound electronic states, it is less effective in describing delocalized electronic states close to or above the vacuum level. As a consequence, Rydberg excitations are not as reliably accounted for. Such states typically require the addition of very diffuse atomic basis functions, causing significant linear dependencies in the molecular basis set, which require careful treatment.[108]

In the *GW*–BSE/MM framework, classical polarization effects of the environment are currently modeled via atomic induced dipoles as described in Sec. III F. This model cannot be expected to yield an accurate description of the response, if the environment is strongly polarizable to the extent that charge flow effects are present. Furthermore, our *GW*–BSE/MM framework relies on the assumption that the environment response is single-reference in character, allowing for an unambiguous identification of the excited states in the self-consistent procedure required to evaluate Eq. (44). This can be achieved by analyzing excited-state characteristics, such as oscillator strengths for optical transitions or the amount of transferred charge between two molecules, or directly the density matrix of the excitation. Any of these state-tracking methods are not straightforwardly applicable, e.g., at or close to intersections where at least two states mix strongly. The inclusion of automatic solutions to this problem[109,110] is left for future developments.

ACKNOWLEDGMENTS

B.B. acknowledges support by the Innovational Research Incentives Scheme Vidi of the Netherlands Organisation for Scientific Research (NWO) (Project No. 723.016.002). Funding is also provided by NWO and the Netherlands eScience Center through Project No. 027.017.G15, within the Joint CSER and eScience program for Energy Research (JCER 2017). We gratefully acknowledge the support of NVIDIA Corporation with the donation of the Titan X Pascal GPU used for this research.

REFERENCES

[1] C. W. Tang and S. A. Vanslyke, Appl. Phys. Lett. **51**, 913 (1987).
[2] C. Adachi, Jpn. J. Appl. Phys., Part 1 **53**, 060101 (2014).
[3] J. J. Halls, C. A. Walsh, N. C. Greenham, E. A. Marseglia, R. H. Friend, S. C. Moratti, and A. B. Holmes, Nature **376**, 498 (1995).
[4] W. Zhao, S. Li, H. Yao, S. Zhang, Y. Zhang, B. Yang, and J. Hou, J. Am. Chem. Soc. **139**, 7148 (2017).
[5] P. Peumans, A. Yakimov, and S. R. Forrest, J. Appl. Phys. **93**, 3693 (2003).
[6] B. E. Logan, Nat. Rev. Microbiol. **7**, 375 (2009).
[7] B. Göhler, V. Hamelbeck, T. Z. Markus, M. Kettner, G. F. Hanne, Z. Vager, R. Naaman, and H. Zacharias, Science **331**, 894 (2011).
[8] C. Risko, M. D. McGehee, and J. L. Brédas, Chem. Sci. **2**, 1200 (2011).
[9] K. Hald, C. Hättig, J. Olsen, and P. Jørgensen, J. Chem. Phys. **115**, 3545 (2001).
[10] K. Hald, P. Jørgensen, J. Olsen, and M. Jaszunski, J. Chem. Phys. **115**, 671 (2001).
[11] K. Andersson, P. A. Malmqvist, B. O. Roos, A. J. Sadlej, and K. Wolinski, J. Phys. Chem. **94**, 5483 (1990).
[12] K. Andersson, P. Å. Malmqvist, and B. O. Roos, J. Chem. Phys. **96**, 1218 (1992).
[13] W. Kohn, Rev. Mod. Phys. **71**, 1253 (1999).
[14] F. Furche and R. Ahlrichs, J. Chem. Phys. **117**, 7433 (2002).
[15] G. Onida, L. Reining, and A. Rubio, Rev. Mod. Phys. **74**, 601 (2002).
[16] Z. L. Cai, K. Sendt, and J. R. Reimers, J. Chem. Phys. **117**, 5543 (2002).
[17] A. Dreuw and M. Head-Gordon, J. Am. Chem. Soc. **126**, 4007 (2004).
[18] S. Kümmel, Adv. Energy Mater. **7**, 1700440 (2017).
[19] L. Hedin and S. Lundqvist, Solid State Physics **23**, 1 (1970).
[20] M. S. Hybertsen and S. G. Louie, Phys. Rev. Lett. **55**, 1418 (1985).
[21] D. Golze, M. Dvorak, and P. Rinke, Front. Chem. **7**, 377 (2019).
[22] Y. Ma, M. Rohlfing, and C. Molteni, Phys. Rev. B **80**, 241405 (2009).
[23] M. Rohlfing, Int. J. Quantum Chem. **80**, 807 (2000).
[24] B. Baumeier, D. Andrienko, Y. Ma, and M. Rohlfing, J. Chem. Theory Comput. **8**, 997 (2012).
[25] B. Baumeier, D. Andrienko, and M. Rohlfing, J. Chem. Theory Comput. **8**, 2790 (2012).
[26] B. Baumeier, M. Rohlfing, and D. Andrienko, J. Chem. Theory Comput. **10**, 3104 (2014).
[27] M. J. Van Setten, F. Weigend, and F. Evers, J. Chem. Theory Comput. **9**, 232 (2013).
[28] M. J. Van Setten, F. Caruso, S. Sharifzadeh, X. Ren, M. Scheffler, F. Liu, J. Lischner, L. Lin, J. R. Deslippe, S. G. Louie, C. Yang, F. Weigend, J. B. Neaton, F. Evers, and P. Rinke, J. Chem. Theory Comput. **11**, 5665 (2015).
[29] D. Varsano, E. Coccia, O. Pulci, A. M. Conte, and L. Guidoni, Comput. Theor. Chem. **1040-1041**, 338 (2014).
[30] D. Golze, J. Wilhelm, M. J. van Setten, and P. Rinke, J. Chem. Theory Comput. **14**, 4856 (2018).

[31] F. Kaplan, M. E. Harding, C. Seiler, F. Weigend, F. Evers, and M. J. Van Setten, J. Chem. Theory Comput. **12**, 2528 (2016).
[32] P. Boulanger, D. Jacquemin, I. Duchemin, and X. Blase, J. Chem. Theory Comput. **10**, 1212 (2014).
[33] D. Jacquemin, I. Duchemin, and X. Blase, J. Chem. Theory Comput. **11**, 3290 (2015).
[34] F. Bruneval, T. Rangel, S. M. Hamed, M. Shao, C. Yang, and J. B. Neaton, Comput. Phys. Commun. **208**, 149 (2016).
[35] G. Strinati, Riv. Nuovo Cimento, Ser. 3 **11**, 1 (1988).
[36] R. W. Godby, M. Schlüter, and L. J. Sham, Phys. Rev. B **37**, 10159 (1988).
[37] M. E. Casida, "Time-dependent density functional response theory for molecules," in *Recent Advances in Density Functional Methods* (World Scientific, 1995), pp. 155–192.
[38] Zenodo votca/xtp v1.6_rc1. (2019); available at https://doi.org/10.5281/zenodo.3563088.
[39] V. Rühle, C. Junghans, A. Lukyanov, K. Kremer, and D. Andrienko, J. Chem. Theory Comput. **5**, 3211 (2009).
[40] V. Rühle, A. Lukyanov, F. May, M. Schrader, T. Vehoff, J. Kirkpatrick, B. Baumeier, and D. Andrienko, J. Chem. Theory Comput. **7**, 3335 (2011).
[41] J. Wehner, L. Brombacher, J. Brown, C. Junghans, O. Çaylak, Y. Khalak, P. Madhikar, G. Tirimbò, and B. Baumeier, J. Chem. Theory Comput. **14**, 6253 (2018).
[42] M. J. Frisch, G. W. Trucks, H. B. Schlegel, G. E. Scuseria, M. A. Robb, J. R. Cheeseman, G. Scalmani, V. Barone, B. Mennucci, G. A. Petersson, H. Nakatsuji, M. Caricato, X. Li, H. P. Hratchian, A. F. Izmaylov, J. Bloino, G. Zhe, G. Zheng, J. L. Sonnenberg, M. Hada, M. Ehara, K. Toyota, R. Fukuda, J. Hasegawa, M. Ishida, T. Nakajima, Y. Honda, O. Kitao, H. Nakai, T. Vreven, J. A. Montgomery, Jr., J. E. Peralta, F. Ogliaro, M. Bearpark, J. J. Heyd, E. Brothers, K. N. Kudin, V. N. Staroverov, R. Kobayashi, J. Normand, K. Raghavachari, A. Rendell, J. C. Burant, S. S. Iyengar, J. Tomasi, M. Cossi, N. Rega, J. M. Millam, M. Klene, J. E. Knox, J. B. Cross, V. Bakken, C. Adamo, J. Jaramillo, R. Gomperts, R. E. Stratmann, O. Yazyev, A. J. Austin, R. Cammi, C. Pomelli, J. W. Ochterski, R. L. Martin, K. Morokuma, V. G. Zakrzewski, G. A. Voth, P. Salvador, J. J. Dannenberg, S. Dapprich, A. D. Daniels, Ö. Farkas, J. B. Foresman, J. V. Ortiz, J. Cioslowski, and D. J. Fox, Gaussian 09, Revision B.01, Gaussian, Inc., Wallingford, CT, 2009.
[43] M. Valiev, E. J. Bylaska, N. Govind, K. Kowalski, T. P. Straatsma, H. J. Van Dam, D. Wang, J. Nieplocha, E. Apra, T. L. Windus, and W. A. De Jong, Comput. Phys. Commun. **181**, 1477 (2010).
[44] F. Neese, Wiley Interdiscip. Rev.: Comput. Mol. Sci. **2**, 73 (2012).
[45] J. Li, G. D'Avino, I. Duchemin, D. Beljonne, and X. Blase, J. Phys. Chem. Lett. **7**, 2814 (2016).
[46] D. Varsano, S. Caprasecca, and E. Coccia, J. Phys. Condens. Matter **29**, 13002 (2017).
[47] J. Li, G. D'Avino, I. Duchemin, D. Beljonne, and X. Blase, Phys. Rev. B **97**, 035108 (2018).
[48] G. Tirimbò, X. de Vries, C. H. L. Weijtens, P. A. Bobbert, T. Neumann, R. Coehoorn, and B. Baumeier, Phys. Rev. B **101**, 035402 (2020).
[49] B. Baumeier, J. Kirkpatrick, and D. Andrienko, Phys. Chem. Chem. Phys. **12**, 11103 (2010).
[50] J. Wehner and B. Baumeier, J. Chem. Theory Comput. **13**, 1584 (2017).
[51] S. Baral, M. Phillips, H. Yan, J. Avenoso, L. Gundlach, B. Baumeier, and E. Lyman, chemRxiv:11347040.v1 (2019).
[52] J. Wehner and B. Baumeier, "Multiscale simulations of singlet and triplet exciton dynamics in energetically disordered molecular systems based on many-body Green's functions theory," New J. Phys. (published online).
[53] D. Chandran and K.-S. Lee, Macromol. Res. **21**, 272 (2013).
[54] W. Li, K. H. Hendriks, M. M. Wienk, and R. A. Janssen, Acc. Chem. Res. **49**, 78 (2016).
[55] K. H. Hendriks, A. S. Wijpkema, J. J. Van Franeker, M. M. Wienk, and R. A. Janssen, J. Am. Chem. Soc. **138**, 10026 (2016).
[56] E. Collado-Fregoso, S. N. Pugliese, M. Wojcik, J. Benduhn, E. Bar-Or, L. Perdigón Toro, U. Hörmann, D. Spoltore, K. Vandewal, J. M. Hodgkiss, and D. Neher, J. Am. Chem. Soc. **141**, 2329 (2019).
[57] W. Kohn and L. J. Sham, Phys. Rev. **140**, A1133 (1965).
[58] L. J. Sham and T. M. Rice, Phys. Rev. **144**, 708 (1966).
[59] L. Hedin, Phys. Rev. **139**, A796 (1965).
[60] W. G. Aulbur, L. Jönsson, and J. W. Wilkins, in *Solid State Physics: Advances in Research and Applications*, edited by H. Ehrenreich and F. Spaepen (Academic Press, 2000), Vol. 54, pp. 1–218.
[61] M. Rohlfing and S. G. Louie, Phys. Rev. B **62**, 4927 (2000).
[62] A. L. Fetter and J. D. Walecka, *Quantum Theory of Many-Particle Systems* (Courier Corporation, 2003).
[63] T. Rangel, S. M. Hamed, F. Bruneval, and J. B. Neaton, J. Chem. Phys. **146**, 194108 (2017).
[64] D. Jacquemin, I. Duchemin, A. Blondel, and X. Blase, J. Chem. Theory Comput. **13**, 767 (2017).
[65] S. Obara and A. Saika, J. Chem. Phys. **84**, 3963 (1986).
[66] S. Reine, T. Helgaker, and R. Lindh, Wiley Interdiscip. Rev.: Comput. Mol. Sci. **2**, 290 (2012).
[67] K. Eichkorn, O. Treutler, H. Öhm, M. Häser, and R. Ahlrichs, Chem. Phys. Lett. **242**, 652 (1995).
[68] X. Blase, C. Attaccalite, and V. Olevano, Phys. Rev. B **83**, 115103 (2011).
[69] J. Laflamme Janssen, B. Rousseau, and M. Côté, Phys. Rev. B **91**, 125120 (2015).
[70] *Strong Coulomb Correlations in Electronic Structure Calculations: Beyond the Local Density Approximation*, edited by V. I. Anisimov (CRC Press, Boca Raton, FL, 2000), p. 33 ff.
[71] M. S. Hybertsen and S. G. Louie, Phys. Rev. B **34**, 5390 (1986).
[72] R. W. Godby and R. J. Needs, Phys. Rev. Lett. **62**, 1169 (1989).
[73] M. Rohlfing, P. Krüger, and J. Pollmann, Phys. Rev. B **52**, 1905 (1995).
[74] F. Weigend and R. Ahlrichs, Phys. Chem. Chem. Phys. **7**, 3297 (2005).
[75] F. Weigend, A. Köhn, and C. Hättig, J. Chem. Phys. **116**, 3175 (2002).
[76] C. Adamo and V. Barone, J. Chem. Phys. **110**, 6158 (1999).
[77] Measured on a single thread of an Intel(R) Xeon(R) CPU E7-4830 v4@2.00GHz.
[78] ISO, ISO\IEC 14882:2014, Information Technology—Programming Languages—C++, International Organization for Standardization, Geneva, Switzerland, 2014.
[79] G. Guennebaud, B. Jacob *et al.*, Eigen v3, http://eigen.tuxfamily.org, 2010.
[80] Intel Math Kernel Library, Reference Manual, Intel Corporation, 2009.
[81] HDF Group, Hierarchical Data Format, version 5, https://www.hdfgroup.org/HDF5/, 1997–2019.
[82] S. Lehtola, C. Steigemann, M. J. Oliveira, and M. A. Marques, SoftwareX **7**, 1 (2018).
[83] B. Schling, *The Boost C++ Libraries* (XML Press, 2011).
[84] D. Luebke, in *2008 5th IEEE International Symposium on Biomedical Imaging: From Nano to Macro* (IEEE, 2008), pp. 836–838.
[85] E. R. Davidson, J. Comput. Phys. **17**, 87 (1975).
[86] J. Demmel, J. Dongarra, A. Ruhe, and H. van der Vorst, in *Templates for the Solution of Algebraic Eigenvalue Problems: A Practical Guide*, edited by Z. Bai (Society for Industrial and Applied Mathematics, Philadelphia, PA, USA, 2000).
[87] E. Vecharynski, J. Brabec, M. Shao, N. Govind, and C. Yang, Comput. Phys. Commun. **221**, 42 (2017).
[88] M. L. Leininger, C. D. Sherrill, W. D. Allen, and H. F. Schaefer, J. Comput. Chem. **22**, 1574 (2001).
[89] R. B. Morgan, Linear Algebra Appl. **154-156**, 289 (1991).
[90] A. Stone, *The Theory of Intermolecular Forces*, 2nd ed. (Oxford University Press, Oxford, 2013), p. 352.
[91] B. T. Thole, Chem. Phys. **59**, 341 (1981).
[92] P. T. Van Duijnen and M. Swart, J. Phys. Chem. A **102**, 2399 (1998).
[93] C. Zhang, C. Lu, Z. Jing, C. Wu, J.-P. Piquemal, J. W. Ponder, and P. Ren, J. Chem. Theory Comput. **14**, 2084 (2018).
[94] C. M. Breneman and K. B. Wiberg, J. Comput. Chem. **11**, 361 (1990).
[95] A. J. Stone, J. Chem. Theory Comput. **1**, 1128 (2005).
[96] K. L. Schuchardt, B. T. Didier, T. Elsethagen, L. Sun, V. Gurumoorthi, J. Chase, J. Li, and T. L. Windus, J. Chem. Inf. Model. **47**, 1045 (2007).
[97] J. Hutter, M. Iannuzzi, F. Schiffmann, and J. VandeVondele, Wiley Interdiscip. Rev.: Comput. Mol. Sci. **4**, 15 (2014).

[98]L. Martínez, R. Andrade, E. G. Birgin, and J. M. Martínez, J. Comput. Chem. **30**, 2157 (2009).
[99]G. Bussi, D. Donadio, and M. Parrinello, J. Chem. Phys. **126**, 014101 (2007).
[100]G. Bussi, T. Zykova-Timan, and M. Parrinello, J. Chem. Phys. **130**, 074101 (2009).
[101]A. Bergner, M. Dolg, W. Küchle, H. Stoll, and H. Preuß, Mol. Phys. **80**, 1431 (1993).
[102]R. Krishnan, J. S. Binkley, R. Seeger, and J. A. Pople, J. Chem. Phys. **72**, 650 (1980).
[103]A. J. Misquitta, R. Podeszwa, B. Jeziorski, and K. Szalewicz, J. Chem. Phys. **123**, 214103 (2005).
[104]S. Baroni, S. de Gironcoli, A. Dal Corso, and P. Giannozzi, Rev. Mod. Phys. **73**, 515 (2001).
[105]F. Giustino, M. L. Cohen, and S. G. Louie, Phys. Rev. B **81**, 115105 (2010).
[106]J. D. Elliott, N. Colonna, M. Marsili, N. Marzari, and P. Umari, J. Chem. Theory Comput. **15**, 3710 (2019).
[107]C. Faber, P. Boulanger, C. Attaccalite, E. Cannuccia, I. Duchemin, T. Deutsch, and X. Blase, Phys. Rev. B **91**, 155109 (2015).
[108]S. Lehtola, J. Chem. Phys. **151**, 241102 (2019).
[109]L. N. Tran, J. A. R. Shea, and E. Neuscamman, J. Chem. Theory Comput. **15**, 4790 (2019).
[110]A. T. B. Gilbert, N. A. Besley, and P. M. W. Gill, J. Phys. Chem. A **112**, 13164 (2008).